*Journal of Naval Architecture and Marine Engineering*
*January 2026*
https://doi.org/10.3329/jname.v23i1.84023 *http://www.banglajol.info*

# NUMERICAL INVESTIGATION OF NON-SIMILAR THERMAL CONVECTION IN BUONGIORNO NANOFLUID WITH DARCY-FORCHHEIMER DRAG USING KELLER BOX METHOD

**Samdani Peerusab [1], Shaik Abdul Gaffar[1], Asra Anjum[1*]**

[1]Sciences and Mathematics Unit, Department of Supportive Requirements, University of Technology and Applied Sciences, Salalah, Sultanate of Oman. P.O. Box 608, PC:211, Salalah, Sultanate of Oman. Email: Samdani.Peerusab@utas.edu.om, abdulsgaffar0905@gmail.com, Abdulgaffar.Shaik@utas.edu.om, asraanjum84@gmail.com*; asra.anjum@utas.edu.om

## Abstract:

*This study investigates non-similar nonlinear thermal convection of a Buongiorno nanofluid through a Darcy–Forchheimer porous medium—an important problem for accurately modelling high-velocity thermal systems where Brownian motion, thermophoresis, and inertial porous-media effects coexist. It further highlights that the governing two-dimensional PDEs are solved using the second-order accurate Keller Box Method, validated against known special cases. The discoveries offer fresh perspectives on the behavior of nanofluids in porous media, contributing to a deeper understanding of heat, mass transfer, and fluid dynamics. It is observed that with increasing Darcy number, there is a substantial hike in velocity, but temperature and concentration decay; conversely, as the Forchheimer number increases, velocity is decreased; however, temperature and concentration profiles are elevated steadily. Specific and quantitative numerical results show that increases in nanoparticle Brownian diffusion Nb elevating temperature profiles by up to ~18% and reducing concentration by ~12%, thermophoresis Nt intensifying thermal fields by ~20% while lowering near-wall velocity, and higher Darcy Da and Forchheimer Fs numbers reducing near-wall momentum by 10–15% but enhancing thermal and concentration layers by up to 17%. This current study has practical implications for enhancing the design and optimization of cooling systems, electronic thermal management, and power systems in situations where accurate temperature regulation and effective heat transport are essential. By addressing the current research gap, this study makes major advances in the fields of thermal sciences and nanofluid technology dynamics, the novelty of simultaneously integrating Buongiorno's nanofluid theory with the nonlinear Da–Fs model in a non-similar convection framework—advancing beyond earlier studies that considered these mechanisms separately and were restricted to ODE formulations.*

***Keywords***: Darcy–Forchheimer; porous medium; non-similar transformations; semi-infinite vertical plate; Brownian motion; buoyancy ratio

## NOMENCLATURE

| | | | |
|---|---|---|---|
| $b$ | Inertial drag coefficient (-) | $Sc$ | *Local Schmidt number (-)* |
| $K$ | permeability (-) | $Sh$ | *Mass transfer rate Sherwood number (-)* |
| $P$ | Pressure (Pa) | $T$ | *Temperature of the fluid (Kelvin)* |
| $C_p$ | Specific heat parameter(J/kgK) | $T_w$ | *Wall temperature (K)* |
| $Cf$ | Skin friction coefficient (-) | $T_\infty$ | *Ambient temperature (K)* |
| $C$ | Concentration (-) | $u, v$ | *Non-dimensional velocity components along the x- and y- directions respectively (m/s)* |
| $C_w$ | Concentration near Wall (-) | $x$ | *Stream-wise coordinate (m)* |
| $C_\infty$ | Concentration in Ambient stream (-) | $y$ | *Transverse coordinate (m)* |
| $D$ | Nanoparticle diffusivity | $V$ | *Velocity vector (m/s)* |

1813-8535 (Print), 2070-8998 (Online)  Received: August, 2025

| | | | |
|---|---|---|---|
| $D_B$ | Brownian diffusion coefficient ($m^2/s$) | ***Greek Symbols*** | |
| *Da* | Darcy number | $\alpha$ (or) $\alpha_m$ | *Thermal diffusivity of the nanofluid ($m^2/s$)* |
| *Dm* | Molecular diffusivity ($m^2/s$) | $\beta$ | *Volumetric expansion coefficient of the fluid (K)* |
| $D_T$ | Thermophoretic diffusion coefficient ($m^2/s$) | $\sigma$ (or) $\sigma_f$ | *The electric conductivity of the fluid (Siemens/m)* |
| *f* | Non-dimensional steam function (-) | | |
| *Fs* | Forchheimer number | $\rho_p$ | *Fluid density of nanoparticles (-)* |
| $f'$ | Nondimensional velocity (-) | $\mu_f$ | *Dynamic viscosity ($kg.m^{-1} \cdot s^{-1}$)* |
| *g* | Acceleration due to gravity ($m/s^2$) | $\nu_f$ | *Kinematic viscosity of base fluid ($m^2/s$)* |
| *Gr* | Grashof number (-) | $\tau$ | *The ratio of the heat capacity of the nanoparticle to the heat capacity of the fluid (-)* |
| *k** | The mean absorption coefficient | $\theta$ | *Dimensionless temperature (-)* |
| | | $\phi$ | *Dimensionless concentration (-)* |
| K | Thermal diffusivity (-) | $\xi$ | *Dimensionless tangential coordinate (-)* |
| $k_m$ | Effective thermal conductivity (W/mK) | $\eta$ | *Dimensionless radial coordinate (-)* |
| *L* | Characteristic length (m) | $\psi$ | *Dimensionless stream function (-)* |
| *Nb* | Brownian motion parameter (-) | $\rho$ (or) $\rho_f$ | *Density of the base fluid (kg/m3)* |
| *Nt* | Thermophoresis parameter (-) | $\rho C_p$ | *Effective heat capacity (J/kg K)* |
| *Nr* | Buoyancy ratio parameter (-) | ***Subscripts*** | |
| *Nu* | Heat transfer rate (Local Nusselt number) (-) | *w* | *Surface conditions* |
| *Pr* | Prandtl number (-) | $\infty$ | *Free stream conditions* |
| | | ***Abbreviations*** | |
| *BL* | Boundary layer | *NPs* | *Nanoparticles* |
| *BLT* | Boundary layer thickness | *NF* | *Nanofluid* |
| *BVP* | Boundary Value Problem | *MHD* | *magnetohydrodynamic* |
| *BNF* | Buongiorno Nanofluid | *KBM* | *Keller Box Method* |
| *BCs* | Boundary Conditions | *(Da-Fs)* | *Darcy-Forchheimer* |

## 1. Introduction

The field of thermal management has witnessed a remarkable surge in interest towards the utilization of nanofluids, which are colloidal suspensions of nanoparticles in base fluids, because these innovative materials exhibit significantly improved thermophysical characteristics when juxtaposed with traditional working fluids, including but not limited to various lubricants, ethylene glycol, and water, thereby making them exceptionally advantageous for enhancing heat transfer processes in a wide array of engineering and industrial applications. The term nanofluid was first introduced by Choi (1995), who demonstrated that dispersing nanoparticles within a base fluid can substantially improve heat transfer performance in cooling processes. Since then, extensive research has examined the influence of various nanoparticle types, including carbides, oxides, and metals, dispersed in different base liquids, using experimental, numerical, or combined approaches. In recent years, substantial progress has been made in the study of diverse nanofluid models, including Williamson NFs (2023), Sutterby NFs (2022), Eyring–Powell NFs (2023), modified Eyring–Powell NFs (2022), and Casson nanoliquids (2022). Anjum *et al*. (2024) analyzed bioconvective nanofluid flow over a stretching surface. Razzaq *et al*. (2021) investigated a non-similar, non-Newtonian Maxwell fluid flow over an exponentially stretching magnetized sheet. Additionally, Cui *et al*. (2021) explored three-dimensional bioconvective nanofluid flow

involving motile nanoparticles and microorganisms. Ali *et al*. (2021) explored boundary layer nanofluid flow over a stretching permeable wedge-shaped surface with magnetic effect.

The thermal behavior and Brownian motion of nanoscale fluid particles described by Buongiorno (2006) form the basis of the Buongiorno nanofluid model. Anjum *et al.* (2025) analyzed Buongiorno-type nanofluid flow over an elongating sheet incorporating multiple slip effects, while Ramesh Reddy *et al.* (2022) explored its transport over a vertical surface, emphasizing Hall and ion-slip influences. A robust mathematical framework for capturing complex interactions during nanofluid film boiling at the vapor–liquid interface was proposed by Yahyaee *et al.* (2024), who demonstrated that the Continuous-Species-Transfer method provides superior accuracy and efficiency for such simulations. Bhavani *et al.* (2024) investigated ultrafast nanofluid velocities essential for safe, non-radiative thermal designs and confirmed that the synthesized nano-coolants exhibit good stability, indicating their potential applicability. Humane *et al.* (2023) examined temperature and solutal effects in a magneto-micropolar nanofluid within an inclined porous stretching surface using the Buongiorno formulation. Wang *et al.* (2023) applied a modified Buongiorno model to study heat and mass transfer in an Ag–$H_2O$ nano-thin film moving through a permeable medium. Katun *et al.* (2021) investigated the numerical modeling of Buongiorno's nanofluid on free convection.

Non-similar transformations represent a sophisticated set of mathematical methodologies that are employed in the intricate analysis of fluid dynamics, particularly in scenarios where the various profiles related to velocity, temperature, or concentration exhibit complex behaviors that preclude their simplification or reduction to a singular, dimensionless similarity form that would allow for easier interpretation and understanding of the underlying physical phenomena involved. Such transformations introduce new variables that capture spatial variations, enabling the treatment of complex flows characterized by non-uniform boundary conditions, variable material properties, or changing geometries. These methods are essential for accurately modeling realistic boundary-layer and heat-transfer problems, where flow characteristics vary along the streamwise direction. Non-similarity may arise from factors such as spatial changes in freestream velocity, variations in wall temperature, surface mass transfer, or fluid injection and suction. To address these challenges, several computational approaches have been developed, including the locally non-similar (LNS) method pioneered by Sparrow *et al.* (1970, 1971), which has since been widely applied to boundary-layer analysis. Razzaq and Farooq (2021) investigated Oldroyd-B fluid flow over an expanding surface under non-similar forced convection. Gaffar *et al.* (2024) studied the effects of Brownian motion, thermophoresis, and mixed convection in nanofluid flow over an isothermal rotating cone. Raees *et al.* (2021) examined non-similar mixed convection in magnetized second-grade nanofluid flow.

Convection flows arise in fluids due to temperature-induced density variations: warmer, lighter fluid rises while cooler, denser fluid sinks, forming continuous circulation patterns that transport heat. These flows are fundamental in atmospheric and oceanic processes and are widely used in engineering systems such as HVAC, geothermal devices, and heat-transfer equipment. Natural convection occurs when buoyancy forces generated by density differences drive the flow, whereas forced convection relies on external mechanisms such as pumps or fans. Mixed convection involves the simultaneous influence of both mechanisms and has been widely examined (e.g., Vedavathi *et al*. 2021; Farooq *et al*. 2021). Convection in porous media is especially important in petroleum and mechanical engineering, with applications in geothermal energy, nuclear waste management, grain drying, enhanced oil recovery, and thermal storage. Usman *et al*. (2024) analyzed natural convection effects in magnetohydrodynamic heat transfer within a wavy cavity, while Shaheen *et al*. (2024) explored the heat-transfer behavior of a hybrid nanofluid flowing over an elongated vertical cylinder.

In fluid dynamics, porosity of the medium is defined as aperture volume divided by the medium's total volume. While there are innumerable naturally existing porous media, some are artificially created to meet industrial needs. Stones such as limestone, sandstone, fabric sponge, human skin, kidney, gall bladder with stones, etc., are examples of naturally permeable media. The substantial need for porous media in manufacturing facilities, several other technical applications have drawn researchers' attention to a deeper examination of the properties and flowing patterns of porous media. Numerous real-world applications can be found in a variety of fields, including the cleansing and purification techniques used in drug manufacturing, the bed-level leaks of water, penetration of porous substances through chemical reactions beneath engineering construction sites, and mass, heat transfer in packed bed reactors. Darcy's law states that "liquid flow through a permeable gravitational force of Earth and stress gradient are directly related to the medium. This law is presented by renowned mathematician and engineer Darcy. However, the medium's porosity increases, and Darcy's resistance causes

viscous shear to expand. When the medium pores are distributed widely and have large pore sizes. In 1901, a Dutch engineer by the name of P. Forchheimer expanded on Darcy's ideas by using them as a foundation. When computing the inertial forces in the momentum equation, Forchheimer (1901) added the square of the velocity term, modifying Darcy's Law. The Forchheimer number provides insight into the relative dominance of inertial forces to viscous forces (governed by viscosity) within the porous medium. Muskat (1946) incorporated this expression into his work; it is now referred to be a "Forchheimer term. Nadeem *et al*. (2021) examined how to optimise the Sisko NF for nonlinear radiative MHD flow and entropy formation across a spinning disc with a non-Darcy porous medium when there is irregular Joule heating, source/sink heat. There are a few more pertinent works by Saeed *et al*. (2020), Khan *et al*. (2024), Makinde *et al*. (2024), and Waqas *et al*. (2023). Hossain *et al*. (2021) studied Unsteady magneto-porous convective transport by micropolar binary fluid due to an inclined plate.

A semi-infinite vertical plate plays an important role in analyzing buoyancy-driven heat and mass transfer relevant to heat exchangers, electronic cooling, building ventilation, atmospheric dispersion, and thermal plumes in oceanography. Gebhart *et al*. (1989) later summarized extensive investigations conducted under various physical conditions, predominantly using air or water as working fluids. In water, density variations depend on both temperature and concentration due to dissolved or suspended materials, giving rise to mass-transfer effects. Numerous studies have since examined convection along semi-infinite vertical plates under different influences (Narahari *et al*., 2018; Amanuallah *et al*., 2018). Although Soret and Dufour effects were once assumed to be negligible in air and water, Gebhart and Pera (1971) showed that coupled mass and heat diffusion can significantly influence density variation, introducing the parameter, $N_r$ to characterize these contributions. Chamkha *et al*. (2010) further analyzed coupled heat–mass transfer over a magnetized, "semi-infinite vertical plate embedded in a porous medium. More recent contributions include Gangadhar *et al*. (2022), who explored EMHD flow of a radiative second-grade nanofluid over a Riga plate using a modified Buongiorno model; Khan *et al*. (2023), who investigated unsteady MHD nanofluid flow past a permeable vertical plate with fractional derivatives; and Anjum *et al*. (2025), who studied dissipative magneto-thermo-convection with Ohmic heating over a semi-infinite vertical surface. Uddin *et al*. (2025) examined the thermal-material transport in boundary-layer flow over a semi-infinite sheet.

In fluid dynamics, the Darcy number is a dimensionless parameter that characterizes the ease with which a fluid moves through a porous medium, defined as the ratio of the medium's permeability to the square of a characteristic length. Named after Henry Darcy, it underpins classical models of flow through porous structures. The Forchheimer number, by contrast, quantifies the relative importance of inertial to viscous forces within porous materials and is commonly used for analyzing flow in packed beds, filters, and porous membranes. The ratio of void volume to total volume is known as porosity. Porous media are made up of solid matrices with interconnected voids. These media can be created for commercial uses or found naturally in things like limestone, sandstone, sponges, skin, and biological organs. Their widespread use in filtration, chemical processing, groundwater flow, geothermal systems, and packed-bed reactors has motivated extensive research into their flow characteristics. Darcy's law relates fluid flow in porous media to pressure gradients and gravitational forces, assuming low velocities and dominant viscous effects. As porosity increases and flow velocities rise, inertial effects become significant, leading Forchheimer (1901) to extend Darcy's law by introducing a velocity-squared term. This modification, later formalized by Muskat (1946), is now known as the Forchheimer term and is essential for modeling high-velocity flows in porous structures. Recent studies continue to apply these concepts in complex systems. Nadeem *et al*. (2021) optimized Sisko nanofluid behavior in nonlinear radiative MHD flow and entropy generation over a rotating disk within a non-Darcy porous medium under irregular Joule heating and heat source/sink effects. Additional relevant contributions include those of Saeed *et al*. (2020), Khan *et al*. (2024), Makinde *et al*. (2024), and Waqas *et al*. (2023).

In the present work, a mathematical model is developed for steady-state laminar boundary layer flow of a Buongiorno nanofluid past a semi-infinite vertical plate with the Da-Fs model, with heat and mass transfer of nanoparticles. Unlike previous studies, which focused on either Da-Fs or Buongiorno's model individually and have been confined to ordinary differential equations. The article fills a critical research gap by integrating the Da-Fs model with BNF theory to study non-similar convection flows.

### 1.1 Novelty of the investigation

The novelty of the present work is that this research simultaneously examines the combined impact of Da-Fsdrag and Buongiorno's nanofluid model within non-similar convection flows adjacent to a semi-infinite vertical plate. This research encompasses fully two-dimensional NF flow partial differential equations and examines velocity, temperature, and concentration profiles using detailed graphs. These have not been considered in previous studies. The novelty of the proposed study renders several key aspects.

- This research offers a more comprehensive understanding by simultaneously incorporating *Nb*, *Nt*, and *Nr* in a *Da*-*Fs* porous medium, unlike existing studies that analyse individual effects by employing robust KBM, known for its superior accuracy, stability, and convergence.
- What influence does the skin friction coefficient have on *Nb*, *Nt*, *Nr*, *Da*, *Fs* compared to the variations observed in Buongiorno's nanofluid past a semi-infinite plate?
- How our findings support the patterns of Reddy *et al*. (2022), (2024), Amanullah *et al*. (2018), and Anjum *et al*. (2025a, 2025b).

The dimensionless nonlinear multi-physical BVP with related wall and free stream BCs is solved employing the robust 2nd order robust implicit finite difference KBM. Validation using previous special instances that have been documented in the literature, and authentication, is also accomplished. Velocity, temperature, and concentration distributions are computed and visualized graphically for the influence of *Nb*, *Nt*, *Nr*, *Da*, and *Fs*. The simulations are relevant and provide an in-depth parametric study, investigating the impact of various factors like permeability, porosity, and the relationship between nanoparticle volume fraction and thermal conductivity affect motion and heat transfer processes. These articles' findings enable precise predictions of heat and mass transmission as well as fluid flow behaviours, which can optimize both cooling systems and power systems through design improvements.

## 2. Mathematical Analysis of Fluid Flow

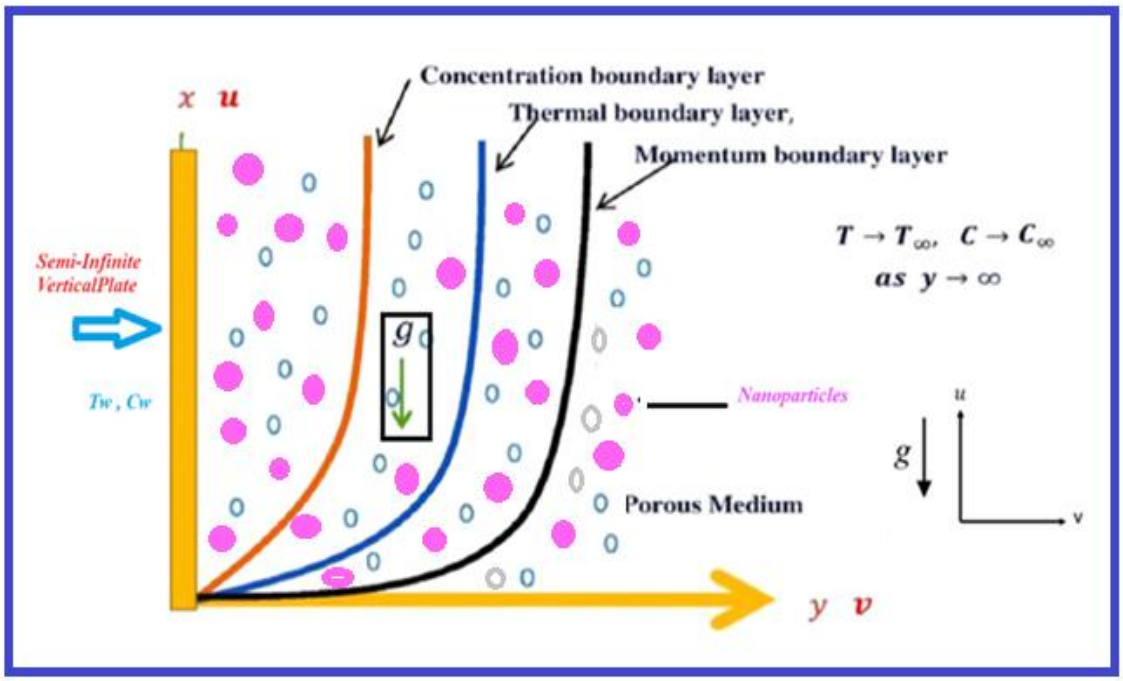


Fig. 1: Physical model and coordinate system

Fig. 1 illustrates a laminar, steady, incompressible natural-convection nanofluid flow over a semi-infinite vertical plate in an xy-coordinate system, where *x* is aligned vertically along the plate and *y* is normal to it. Buoyancy forces arise from thermal and concentration gradients in the suspended species, driving the upward flow. As the Grashof number becomes very large, the Navier–Stokes equations reduce to the classical boundary-layer form. Gravity $g$ acts downward, opposing the buoyant motion. Initially, both the nanofluid and the plate are maintained at uniform temperature and concentration; far from the plate, the fluid reaches constant ambient

values. The porous medium is assumed homogeneous and isotropic to simplify its effective thermal conductivity. The flow resistance within the medium follows the modified, second-order Darcy–Forchheimer model, in which the pressure gradient incorporates both viscous (Darcy) and inertial (Forchheimer) contributions.

$$\nabla_p = -aU + bU^2 \tag{1}$$

Where $\nabla_p$ is the pressure, $a = \frac{\mu}{K}$ *and* $b = \frac{\rho}{K_1}$ are the constants, and *U* is velocity. The governing equations for mass, momentum, energy, and nanoparticle species (concentration) for the Buongiorno nanofluid under the boundary layer and Boussinesq approximations may be established using the models of Buongiorno (2006), Reddy *et al*. ((2022), (2024)), Amanullah *et al*. (2018), and Anjum *et al*. (2025a, 2025b)**.**

The vectorial forms of the conservation equations are:

$$\nabla . \boldsymbol{V} = 0 \tag{2}$$

$$\rho_f \left( \frac{\partial V}{\partial t} + V.\nabla V \right) = -\nabla p + \mu_f \left( \nabla^2 \boldsymbol{V} \right) + g\left[ (1 - C_\infty) \rho_{f\infty} \beta (T - T_\infty) - (\rho_p - \rho_{f\infty})(C - C_\infty) \right] \tag{3}$$

$$(\rho c)_p \left( \frac{\partial T}{\partial t} + V.\nabla \mathrm{T} \right) = k_m \nabla^2 T + (\rho c)_p \left[ D_B \nabla C.\nabla T + \frac{D_T}{T_\infty} (\nabla T)^2 \right] \tag{4}$$

$$\frac{\partial C}{\partial t} + \frac{1}{\varepsilon} \mathrm{V}.\nabla C = D_m \nabla^2 C + \frac{D_T}{T_\infty} \nabla^2 T \tag{5}$$

Here $V = (u, v)$ is the velocity vector

The Semi-infinite substrate surface (wall) and free stream (boundary layer edge) are subject to the following BCs, Reddy *et al*. (2022), (2024), and Anjum *et al*. (2025a, 2025b):

$$\begin{aligned} &u = v = 0, \quad T = T_w, \quad C = C_w && at \quad y = 0 \\ &u \to 0, \quad T \to T_\infty, \quad C \to C_\infty && as \quad y \to \infty \end{aligned} \tag{6}$$

Equation (3) can be expressed as follows in accordance with Kuznetsov and Nield (2010), given the low concentration of NPs and the use of a suitable pressure:

$$\rho_f \left( \frac{\partial V}{\partial t} + V.\nabla V \right) = -\nabla p + \mu_f \left( \nabla^2 \boldsymbol{V} \right) + g\left[ (1 - C_\infty) \rho_{f\infty} \beta (T - T_\infty) - (\rho_p - \rho_{f\infty})(C - C_\infty) \right]$$

The Oberbeck-Boussinesq approximations yield the linearized momentum equation, which is as follows:

$$0 = -\nabla p + \mu_f \left( \nabla^2 V \right) + g\left[ (1 - C_\infty) \rho_{f\infty} \beta (T - T_\infty) - (\rho_p - \rho_{f\infty})(C - C_\infty) \right] \tag{7}$$

The reduced boundary layer equations are used by Reddy *et al*. (2022), (2024), and Anjum *et al*.(2025a, 2025b)**.**

$$\frac{\partial u}{\partial x} + \frac{\partial v}{\partial y} = 0 \tag{8}$$

$$u \frac{\partial u}{\partial x} + v \frac{\partial u}{\partial y} = \nu \frac{\partial^2 u}{\partial y^2} + g\left[ (1 - C_\infty) \rho_{f\infty} \beta (T - T_\infty) - (\rho_p - \rho_{f\infty})(C - C_\infty) \right] - \frac{\nu}{K} u - \frac{b}{K} u^2 \tag{9}$$

$$u \frac{\partial T}{\partial x} + v \frac{\partial T}{\partial y} = \alpha_m \frac{\partial^2 T}{\partial y^2} + \tau \left[ D_B \frac{\partial T}{\partial y} \frac{\partial C}{\partial y} + \frac{D_T}{T_\infty} \left( \frac{\partial T}{\partial y} \right)^2 \right] \tag{10}$$

$$\frac{1}{\varepsilon} \left( u \frac{\partial C}{\partial x} + v \frac{\partial C}{\partial y} \right) = D_m \frac{\partial^2 C}{\partial y^2} + \frac{D_T}{T_\infty} \frac{\partial^2 T}{\partial y^2} \tag{11}$$

Where $\alpha_m = \frac{k_m}{(\rho c)_f}, \quad \tau = \frac{(\rho c)_p}{(\rho c)_f}$ (12)

The relevant boundary conditions imposed at the plate surface and in the free stream, Reddy *et al*. (2022), (2024), and Anjum *et al*.(2025a, 2025b):

$$u = v = 0, \quad T = T_w, \quad C = C_w \qquad at \quad y = 0$$
$$u \to 0, \quad T \to T_\infty, \quad C \to C_\infty \qquad as \quad y \to \infty \tag{13}$$

$$\xi = \left(\frac{x}{L}\right)^{\frac{1}{2}}, \quad \eta = C_1 y x^{\frac{-1}{4}}, \quad \psi = 4\nu C_1 x^{\frac{3}{4}} f(\xi,\eta), \quad C_1 = \left(\frac{Gr}{4}\right)^{\frac{1}{4}} L^{\frac{-3}{4}} \tag{14}$$

$$Gr = \frac{g\beta(1-C_\infty)\rho_{f\infty}(T_w - T_\infty)L^3}{4\nu^2}, \; \theta(\xi,\eta) = \frac{T - T_\infty}{T_w - T_\infty}, \; \phi(\xi,\eta) = \frac{C - C_\infty}{C_w - C_\infty}$$

Stream function $\psi$ is defined as $u = \frac{\partial \psi}{\partial y}$ *and* $v = -\frac{\partial \psi}{\partial x}$

Subject to the velocity components given in terms of stream function, equation (8) is automatically satisfied. The dimensionless scaling variables listed below are introduced: Equations (9–11) provide the following paired nonlinear ordinary differential boundary layer equations:

$$f''' + 3ff'' - 2f'^2 + (\theta - Nr\phi) - \frac{\xi}{DaGr^{\frac{1}{2}}} f' - \frac{Fs}{Da}\xi^2 f'^2 = 2\xi\left(f'\frac{\partial f'}{\partial \xi} - f''\frac{\partial f}{\partial \xi}\right) \tag{15}$$

$$\frac{\theta''}{\Pr} + 3f\theta' + Nb\theta'\phi' + Nt\theta'^2 = 2\xi\left(f'\frac{\partial \theta}{\partial \xi} - \theta'\frac{\partial f}{\partial \xi}\right) \tag{16}$$

$$\frac{\phi''}{Sc} + 3f\phi' + \frac{1}{Sc}\frac{Nt}{Nb}\theta'' = 2\xi\left(f'\frac{\partial \phi}{\partial \xi} - \phi'\frac{\partial f}{\partial \xi}\right) \tag{17}$$

The transformed non-dimensional boundary conditions are Anjum *et al.* (2025a, 2025b):

$$f = 0, \quad f' = 0, \quad \theta = 1, \quad \phi = 1 \quad at \quad \eta = 0$$
$$f' \to 0, \quad \theta \to 0, \quad \phi \to 0 \qquad as \quad \eta \to \infty \tag{18}$$

The nondimensional parameters are Reddy *et al.* (2022), (2024), and Anjum *et al.* (2025a, 2025b):

$$Nr = \frac{(\rho_p - \rho_{f\infty})(C_w - C_\infty)}{\rho_{f\infty}(1-C_\infty)\beta(T_w - T_\infty)}, \quad Nb = \frac{\tau D_B (C_w - C_\infty)}{\nu}, \; Nt = \frac{\tau D_T (T_w - T_\infty)}{\nu T_\infty}$$

$$Gr = \frac{(1-C_\infty)\rho_{f\infty} g\beta(T_w - T_\infty)L^3}{4\nu^2}, \; Da = \frac{K}{2L^2}, \; Fs = \frac{2b}{L}, \; \Pr = \frac{\nu}{\alpha_m}, \; Sc = \frac{\nu}{D_m}$$

## 2.1 Quantities of physical importance

The shear stress components at the surface, known as the skin-friction coefficients $C_f$) the heat transfer rate known as the Nusselt number *Nu*, and the mass transfer rate of NPs, known as the Sherwood number *Sh*, are the physically key interesting engineering design parameters for the Semi-infinite vertical surface Reddy *et al*., 2024; Anjum *et al*.(2025a, 2025b)**.** They are defined as follows:

$$\frac{1}{4\nu\mu C_1^3 x^{\frac{1}{4}}} C_f = f''(\xi, 0) \tag{19}$$

$$\frac{-1}{k\Delta T C_1 x^{\frac{-1}{4}}} Nu = \theta'(\xi, 0) \tag{20}$$

$$\frac{-1}{D\Delta C C_1 x^{\frac{-1}{4}}} Sh = \phi'(\xi, 0) \tag{21}$$

$$\Delta T = T_w - T_\infty, \quad \Delta C = C_w - C_\infty \tag{22}$$

Here, $\xi \sim 0$ and the BLEs (15) – (17) contract to a system of ODEs in the neighborhood of the lower stagnation point:

$$f''' + 3ff'' - 2f'^2 + (\theta - Nr\phi) - \frac{\xi}{Da\,Gr^{\frac{1}{2}}} f' - \frac{Fs}{Da}\xi^2 f'^2 = 0$$

$$\frac{\theta''}{\Pr} + 3f\theta' + Nb\,\theta'\phi' + Nt\,\theta'^2 = 0$$

$$\frac{\phi''}{Sc} + 3f\phi' + \frac{1}{Sc}\frac{Nt}{Nb}\theta'' = 0$$

## 2.2 KBM solution and validation

The dimensionless BLEs (15) – (17) have been numerically solved using the Keller box implicit finite difference scheme (1978). This approach retains its status as one of the leading numerical methods to solve two-point BVPs. The Keller-box approach offers appealing extrapolation "properties and second-order accuracy with flexible spacing. On a rectangular grid (Fig. 2 ), a finite-difference technique is used ("box") and converts the partial differential equations of BL into an algebraic set of equations. It attains remarkable accuracy, offers steady numerical meshing characteristics, and converges quickly. By utilizing fully implicit methods with customizable stepping, the Keller box approach improves accuracy on explicit or semi-implicit schemes. Another advantage of this method is that two-coordinate ($\xi$, $\eta$) nonlinear partial differential equation systems can be easily accommodated, unlike other solvers, such as MATLAB BVP4C, which are restricted to ordinary differential boundary value problems. In line with the physics of parabolic systems, each discretization step is fully coupled. The discrete algebra connected to the Keller-Box technique is essentially independent of any other mimicking (physics-capturing) computation methods (2020), (2024), (2013), Reddy *et al.* (2024), Hussain *et al.* (2023).

The four phases involved in the KBM scheme:

1. The *Nth* order PDE system is divided into *N* first-order ODEs.
2. Discretisation of Finite Differences.
3. Keller algebraic equations that are non-linear can be quasi-linearized.
4. The linearised Keller Algebraic Equations' block-tridiagonal elimination solution.

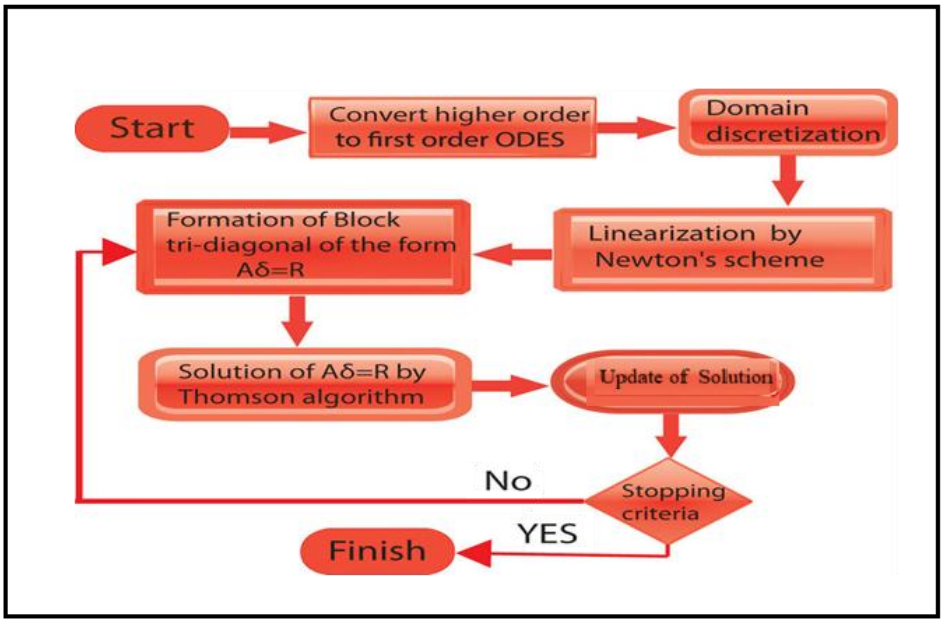


Fig. 2: Keller box method flow chart.

## Step 1: The Nth order PDE system is divided into N first-order ODEs

Equations (15) - (17) and BCs (18) are utilized in conjunction with additional variables to convert the BVP into a multiple system of first-order equations. Consequently, a set of nine simultaneous first-order ODEs is produced by adding the additional variables Anjum *et al.* (2025a), (2025b):

$$u(x,y)=f',\ v(x,y)=f'',\ g'(x,y)=p,\ s(x,y)=\theta,\ t(x,y)=\theta' \tag{23}$$

$$f'=u \tag{24}$$

$$u'=v \tag{25}$$

$$g'=p \tag{26}$$

$$s'=t \tag{27}$$

$$v'+3fv-2u^2+(s-Nr\,g)-\frac{\xi}{Da\sqrt{Gr}}(u)-\frac{Fs}{Da}\xi^2u^2=2\xi\left[u\frac{\partial u}{\partial\xi}-v\frac{\partial f}{\partial\xi}\right] \tag{28}$$

$$\frac{t'}{\Pr}+3ft+Nb\,t\,p+Nt\,t^2=2\xi\left(u\frac{\partial s}{\partial\xi}-t\frac{\partial f}{\partial\xi}\right) \tag{29}$$

$$\frac{p'}{Sc}+3fp+\frac{1}{Sc}\frac{Nt}{Nb}t'=2\xi\left(u\frac{\partial g}{\partial\xi}-p\frac{\partial f}{\partial\xi}\right) \tag{30}$$

where differentiation concerning $\eta$ is indicated by primes. Regarding the dependent variables, the BCs turn into:

$$f=0,\quad f'=0,\quad \theta=1,\quad \phi=1\quad at\quad \eta=0$$
$$f'\to 0,\quad \theta\to 0,\quad \phi\to 0\quad as\quad \eta\to\infty$$

## Step 2: Discretization of Finite Differences

In a Keller box (cell), Fig. 3 a 2D computational grid is imposed in the $\xi$-$\eta$ plane**.** The stepping process is defined by:

$$\eta_0=0,\qquad \eta_j=\eta_{j-1}+h_j,\qquad j=1,2,\ldots,J,\qquad \eta_J\equiv\eta_\infty \tag{31}$$

$$\xi^0=0,\qquad \xi^n=\xi^{n-1}+k_n,\qquad n=1,2,\ldots,N \tag{32}$$

where $k_n$ is the $\Delta\xi$ - spacing and $h_j$ is the $\Delta\eta$ - spacing. If $g_j^n$ denotes the value of any variable at $(\eta_j,\xi^n)$, then the variables and derivatives of Equations (24) – (30) at $(\eta_{j-1/2},\ \xi^{n-1/2})$ are replaced by":

$$g_{j-1/2}^{n-1/2}=\frac{1}{4}\left(g_j^n+g_{j-1}^n+g_j^{n-1}+g_{j-1}^{n-1}\right) \tag{33}$$

$$\left(\frac{\partial g}{\partial\eta}\right)_{j-1/2}^{n-1/2}=\frac{1}{2h_j}\left(g_j^n-g_{j-1}^n+g_j^{n-1}-g_{j-1}^{n-1}\right) \tag{34}$$

$$\left(\frac{\partial g}{\partial\xi}\right)_{j-1/2}^{n-1/2}=\frac{1}{2k^n}\left(g_j^n-g_{j-1}^n+g_j^{n-1}-g_{j-1}^{n-1}\right) \tag{35}$$

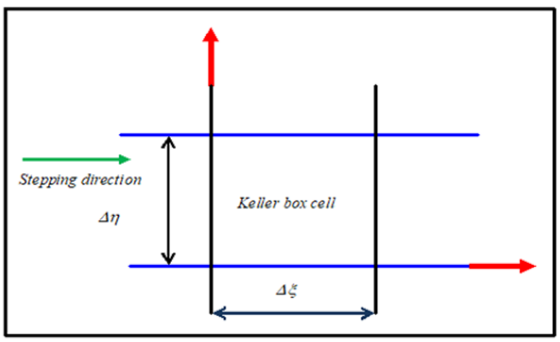


Fig. 3: Two-dimensional computational grid

Equations (24) through (30) and their corresponding finite-difference approximation for the middle point $\left(\eta_{j-1/2},\ \xi^{n}\right)$, are:

$$h_j^{-1}\left(f_j^n - f_{j-1}^n\right) = u_{j-1/2}^n \tag{36}$$

$$h_j^{-1}\left(u_j^n - u_{j-1}^n\right) = v_{j-1/2}^n \tag{37}$$

$$h_j^{-1}\left(g_j^n - g_{j-1}^n\right) = p_{j-1/2}^n \tag{38}$$

$$h_j^{-1}\left(s_j^n - s_{j-1}^n\right) = t_{j-1/2}^n \tag{39}$$

$$\begin{aligned}&\left(v_j - v_{j-1}\right) + \frac{h_j}{4}(3+2\alpha)\left(f_j + f_{j-1}\right)\left(v_j + v_{j-1}\right) + \frac{h_j}{2}\left(s_j + s_{j-1} - Nr\left(g_j + g_{j-1}\right)\right)\\ &-2\left(1+\alpha - \frac{Fs}{Da}\xi^2\right)\frac{h_j}{4}\left(u_j + u_{j-1}\right)^2 - \frac{\xi}{Da\sqrt{Gr}}\frac{h_j}{2}\left(u_j + u_{j-1}\right) - \alpha h_j f_{j-1/2}^{n-1}\left(v_j + v_{j-1}\right)\\ &-\alpha h_j v_{j-1/2}^{n-1}\left(f_j + f_{j-1}\right) - v^{n-1} = \left[R_1\right]_{j-/12}^{n-1}\end{aligned} \tag{40}$$

$$\frac{1}{\Pr}\left(t_j - t_{j-1}\right) + \frac{h_j}{4}(3+2\alpha)\left(f_j + f_{j-1}\right)\left(t_j + t_{j-1}\right) + Nb\frac{h_j}{4}\left(t_j + t_{j-1}\right)\left(p_j + p_{j-1}\right) + Nt\frac{h_j}{4}\left(t_j + t_{j-1}\right)^2 \tag{41}$$

$$-2\frac{\alpha h_j}{4}(su)_{j-1/2}^{n-1} + \alpha h_j\begin{pmatrix} s_{j-1/2}^{n-1}\left(u_j + u_{j-1}\right) - u_{j-1/2}^{n-1}\left(s_j + s_{j-1}\right) - f_{j-1/2}^{n-1}\left(t_j + t_{j-1}\right) + \\ t_{j-1/2}^{n-1}\left(f_j + f_{j-1}\right)\end{pmatrix} = \left[R_2\right]_{j-1/2}^{n-1}$$

$$\begin{aligned}&\frac{1}{Sc}\left(p_j - p_{j-1}\right) + \frac{1}{Sc}\frac{Nt}{Nb}\left(t_j - t_{j-1}\right) + \frac{h_j}{4}(3+2\alpha)\left(f_j + f_{j-1}\right)\left(p_j + p_{j-1}\right)\\ &-2\frac{\alpha h_j}{4}(ug)_{j-1/2}^{n-1} + 2\frac{\alpha h_j}{2}\begin{pmatrix} g_{j-1/2}^{n-1}\left(u_j + u_{j-1}\right) - u_{j-1/2}^{n-1}\left(g_j + g_{j-1}\right) - f_{j-1/2}^{n-1}\left(p_j + p_{j-1}\right) + \\ p_{j-1/2}^{n-1}\left(f_j + f_{j-1}\right)\end{pmatrix} = \left[R_3\right]_{j-1/2}^{n-1}\end{aligned} \tag{42}$$

where we have used the abbreviations

$$\left[R_1\right]_{j-1/2}^{n-1} = -h_j\begin{bmatrix}\left(v'\right)_{j-1/2}^{n-1} + (3-2\alpha)\left(f\,v\right)_{j-1/2}^{n-1} + \left(s_{j-1}^{n-1} - Nr\,g_{j-1}^{n-1}\right) - \frac{\xi}{Da\sqrt{Gr}}\left(u_{j-1}^{n-1}\right) + \\ \left(2 - 2\alpha - \frac{Fs}{Da}\right)\left(u_{j-1}^{n-1}\right)^2\end{bmatrix} \tag{43}$$

$$\left[R_2\right]_{j-1/2}^{n-1} = -h_j\left[\frac{1}{\Pr}\left(t'\right)_{j-1/2}^{n-1} + (3-2\alpha)\left(ft\right)_{j-1/2}^{n-1} + Nb\left(tp\right)_{j-1/2}^{n-1} + Nt\left(t^2\right)_{j-1/2}^{n-1} + 2\alpha\left(us\right)_{j-1/2}^{n-1}\right] \tag{44}$$

$$\left[R_3\right]_{j-1/2}^{n-1} = -h_j\left[\frac{1}{Sc}\left(p'\right)_{j-1/2}^{n-1} + \frac{1}{Sc}\frac{Nt}{Nb}\left(t'\right)_{j-1/2}^{n-1} + (3-2\alpha)\left(fp\right)_{j-1/2}^{n-1} + 2\alpha\left(ug\right)_{j-1/2}^{n-1}\right] \tag{45}$$

The BCs are:

$$f_0^n = 0,\ u_0^n = 0,\ g_0^n = 0,\ \ s_0^n = 0,\ u_J^n = 0,\ g_J^n = 0,\ s_J^n = 0 \tag{46}$$

## Stage 3: Keller's non-linear algebraic equations can be quasi-linearized.

If we presume $f_j^{n-1}, u_j^{n-1}, v_j^{n-1}, g_j^{n-1}, p_j^{n-1}, s_j^{n-1}, t_j^{n-1}$ to be widely recognized for $0 \le j \le J$, the consequence is in a framework of *7J+7* equations for the solution of *7J+7* unknowns $f_j^n, u_j^n, v_j^n, g_j^n, p_j^n, s_j^n, t_j^n\ \ j = 0,1,2,\ldots,J$. This non-linear system of algebraic equations is linearized by means of Newton's method.

## Stage 4: The linearized Keller Algebraic Equations' block-tridiagonal elimination solution.

Since the linearized system has a block-tridiagonal structure, it is solved using the block-elimination technique. This results in a block-tridiagonal architecture composed of block matrices. Every component of the coefficient matrix is a matrix in and of itself, and the full linearized system is represented as a block matrix framework. This system is solved using the efficient Keller-box approach. A significant influence on the numerical output is the quantity of mesh points in both axes. After a few experiments, a larger number of mesh points are selected in the radial coordinate ($\eta$-direction), whereas a significantly lesser number are employed in the tangential coordinate ($\xi$-direction). $\eta_{\max}$ = 10 establishes an appropriately high level at which the desired BCs are accomplished. For this flow domain, $\xi_{max}$ is set as 3. In the current computation, mesh independence is attained. The computational algorithm is run on a PC using MATLAB. As explained by Keller (1978), the procedure exhibits outstanding stability, convergence, and consistency.

## 2.3 Convergence analysis

Until a certain convergence threshold is met, computations are performed. Laminar boundary-layer calculations commonly use the wall shear stress parameter, $v$ ($\xi$, 0), as the convergence criterion Beg (2013). The most significant error in BL calculations is found to be in the wall shear stress parameter. It is important to note that this convergence criterion is applied throughout the study since it is effective, appropriate, and the best solution to all of the issues. The computations are terminated when $\left|\delta v_0^{(i)}\right| \prec \varepsilon_1$, a modest $\varepsilon_1$ specified value is reached.

## 2.4 Validation of Keller box code

The Nusselt number *Nu* for Prandtl numbers *Pr* is compared to those published in previous studies to assess the validity of the present numerical code. Table 1 illustrates this by comparing the validity of the current research with that of previous investigations. The data confirms that the present results validate and reinforce the findings of previous studies, indicating strong agreement and reliability in the observed trends. Error analysis Percentage of the comparisons is also included.

Table 1 Local skin friction coefficient $C_f$ comparison for different values of $\xi$ *as* $Da \to \infty$, $Fs=0$.

| | **Local skin friction coefficient $C_f$** | | | | |
|---|---|---|---|---|---|
| $\xi$ | **Saddiqa *et al.* (2021)** | **Ramesh Reddy *et al.* (2022)** | **Current Results** | **Error Analysis% with (2021)** | **Error Analysis% With (2022)** |
| **0.1** | 0.014 | 0.012 | 0.016 | 2% | 4% |
| **0.2** | 0.050 | 0.049 | 0.054 | 4% | 5% |
| **0.3** | 0.104 | 0.103 | 0.106 | 2% | 3% |
| **0.4** | 0.172 | 0.171 | 0.169 | 3% | 2% |
| **0.5** | 0.250 | 0.249 | 0.251 | 1% | 2% |
| **0.6** | 0.336 | 0.338 | 0.339 | 3% | 1% |
| **0.7** | 0.430 | 0.429 | 0.432 | 2% | 3% |
| **0.8** | 0.529 | 0.528 | 0.531 | 2% | 3% |
| **0.9** | 0.634 | 0.634 | 0.634 | 0% | 0% |
| **1** | 0.744 | 0.743 | 0.747 | 3% | 4% |
| **1.1** | 0.858 | 0.857 | 0.860 | 2% | 3% |
| **1.2** | 0.975 | 0.971 | 0.975 | 0% | 4% |
| **1.4** | …… | …… | 0.998 | | |

## 3. Numerical Results and Discussion

This part focuses on the results that were obtained and the physical discussions that followed. This section has been split into the following two subsections:

### 3.1 Parameter's effect on velocity, temperature, and concentration profiles

The present section highlights the physical perspective of Buongiorno's Nanofluid flow past a semi-infinite vertical plate with the Da-Fs model. The Keller-box finite difference technique is applied for equations (15) – (17). A detailed graphical illustration for the solution is shown in Figures (2 – 11) utilizing MATLAB Code, on Velocity $f'$, Temperature $\theta$ and nanoparticle volume fraction concentration $\phi$, shear stress rate $C_f$, heat transfer rate Nusselt number $Nu$ nanoparticle mass transfer rate Sherwood number $Sh$for six dimensionless thermophysical parameters in the model, such as $Nb$, $Nt$, $Nr$, $Da$, $Fs$ are presented along the radial coordinate ($\eta$). The Numerical problem comprises two independent space variables ($\xi,\eta$), default values of the following variables are $Pr$ =0.71, $Sc$ = 0.6, $Nr$ =0.1, $Nb$ = $Nt$= 0.3, $Da$ = $Fs$ =0.5, $Gr$ = 10, $\xi$ = 1.0 are prescribed.

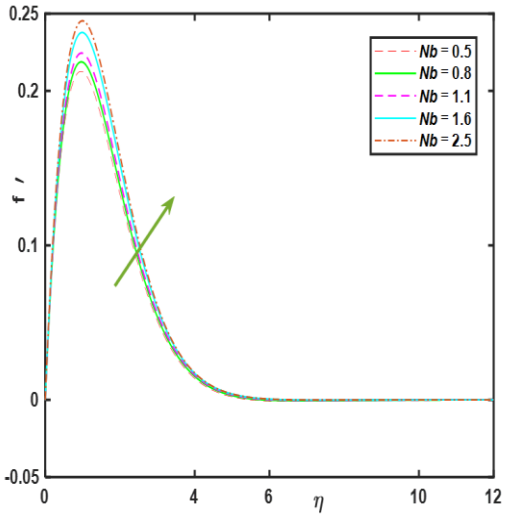


Fig. 4: Velocity description for *Nb*.

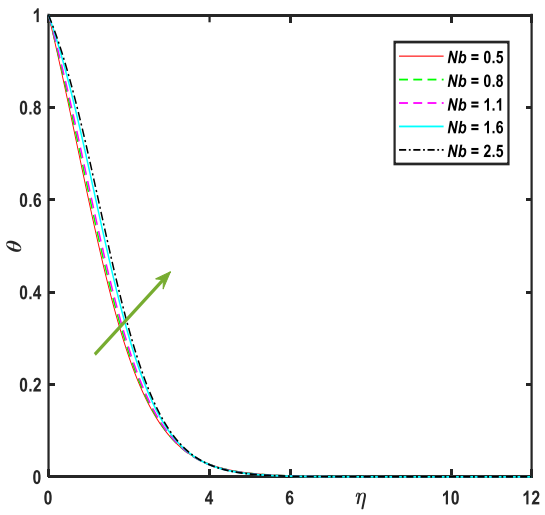


Fig. 5: Temperature description for *Nb*.

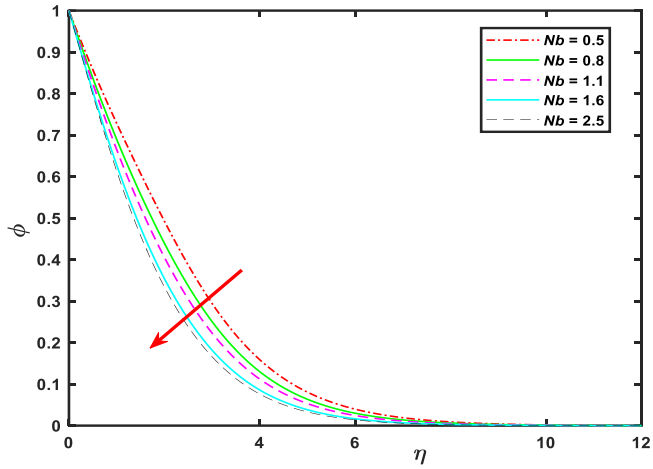


Fig. 6: Concentration description for Nb.

Figures (4 – 6) show the impact of Brownian motion $Nb$ on $f'$, $\theta$ ($\phi$ profiles through the surface regime with transverse coordinate ($\eta$). In Fig. 4 , $f'$ is enhanced, although a stronger elevation is computed in the former with greater $Nb$ values. $Nb$ also modifies the NF thermal conductivity and the propensity for heat transmission in the NF. As a result, the increased random motion of the NPs modifies the thermal behaviour as well, and the momentum field experiences this influence through thermal buoyancy. As $Nb$ increases, $\theta$ is positively affected across the BL regime, as seen in Fig. 5 . There is also a significant change in the topology $\theta$ profiles further

from the substrate (wall) at very high *Nb* values. Raising the $\theta$ aggravates the motion of the NPs and ballistic collisions. Consequently, chaotic Brownian motion is increased even further. The increased heat conduction in the regime and the improved micro-convection surrounding the NPs are also influenced by the change in thermal conductivity with greater *Nb* values. This results in a thicker thermal BL due to a heating effect. Although the fluid's molecules and NPs are always moving, there is a noticeable shift in $\theta$ overall. Brownian motion, however, predominates in the random thermal motion of the NPs. As *Nb* is increased, however, the intensification in ballistic collisions curtails the diffusion of NPs, and this produces a notable decrease in($\phi$ values, as observed in Fig. 6 . Hence, the thickness of nanoparticle concentration BL is reduced, which is important in fine-tuning coating structure during the manufacturing process. Our results concur with the trends of Reddy *et al*. (2022), Anjum *et al*. (2025a), (2025b), who have also shown that the greater viscosity acts to accelerate the flow and heat convection but depresses mass transfer rates. The physical significance of these observations lies in the complex interplay between Brownian motion and NF dynamics. As *Nb* increases, nanoparticles experience enhanced random movement, facilitating more efficient thermal diffusion and increasing fluid velocity. This phenomenon is crucial in settings where efficient heat transport is necessary, like cooling structures and thermal management in engineering.

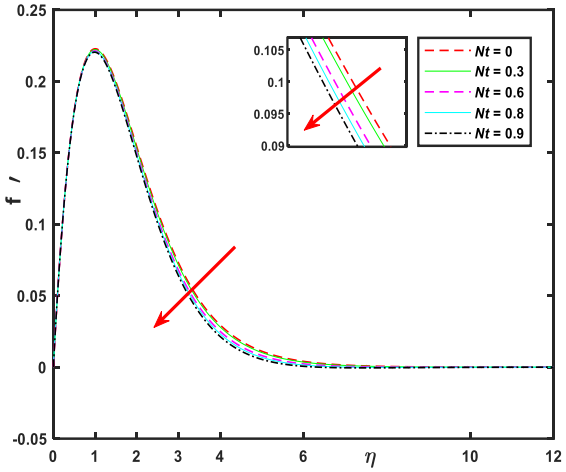


Fig. 7: Velocity description for *Nt*

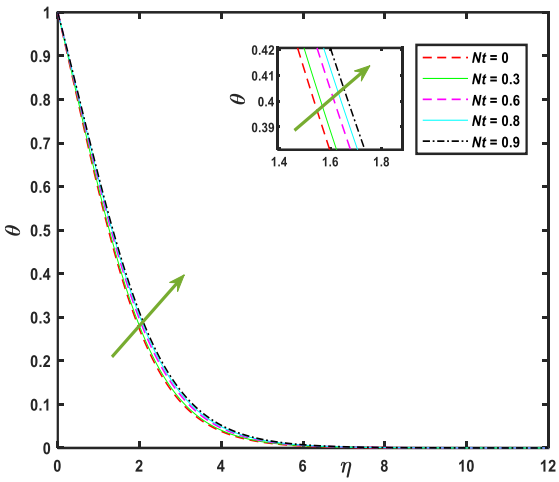


Fig. 8: Temperature description for *Nt*

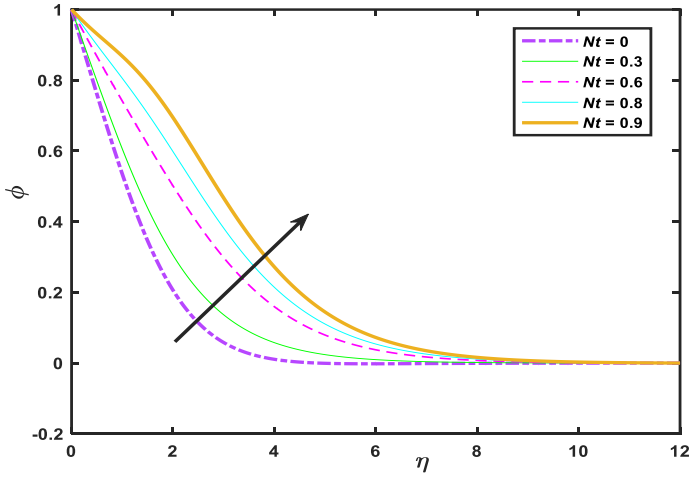


Fig. 9: Concentration description for *Nt*

Figures (7–9) depict the influence of the thermophoresis parameter *Nt* on *f'* $\theta$, $\phi$ profiles. From Fig. 7, an increase in *Nt* decelerates velocity *f'*. The increasing thermophoresis parameter value enhances temperature $\theta$ in Fig. 8 and considerably boosts concentration $\phi$ in Fig. 9 . These trends are sustained at all distances, transversed to the inclined substrate. However, while asymptotic decays occur from the wall to the free stream for all $\theta$ profiles, the nanoparticle concentration profile is only a decay for *Nt* = 0, which has not been identified previously in the literature. As *Nt* increases, the topology is flipped from a convex to a concave one for *Nt* = 0.2.

With subsequent elevation in the thermophoresis parameter, a peak in $\phi$emerges progressively further from the wall. Eventually, however, profiles for $Nt > 0.2$ do descend smoothly to the free stream. Overall, stronger thermophoresis elevates the thermal and nanoparticle species BLT. The impact of a higher thermophoretic temperature gradient is clearly significant on all transport characteristics, confirming the important role it plays in NF mechanics. Our findings support the patterns of Reddy *et al*. (2022), Anjum *et al*. (2025a), and (2025b). Physical interpretation: This signifies that a stronger thermophoretic force leads to enhanced momentum, heat, and mass transfer, reflecting more pronounced thermal and solute gradients in the NF flow. The two most intriguing aspects of Buongiorno's nanofluid model are thermophoresis and Brownian motion characteristics. In essence, these characteristics raise the fluid's temperature, which is essential for optimizing heat and mass transfer processes in various applications.

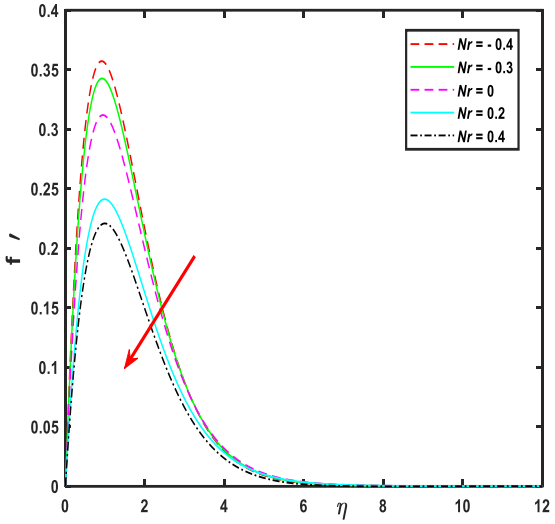


Fig.10: Velocity description for *Nr*.

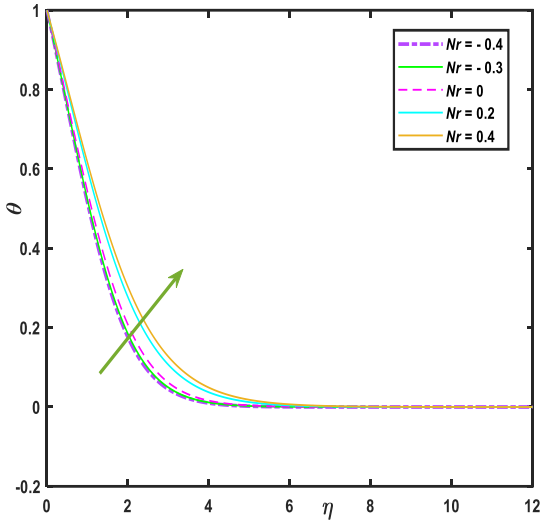


Fig. 11: Temperature description for *Nr*.

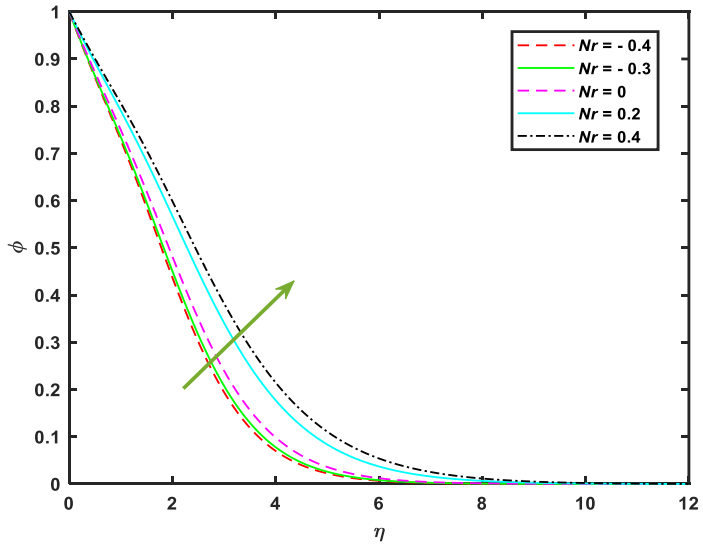


Fig. 12: Concentration description for *Nr*.

Figures (10–12) elucidate the impact of the combined Buoyancy ratio parameter *Nr* on profiles $f'$, $\theta$, $\phi$ As seen in Fig. 10, velocity $f'$ is suppressed with positive *Nr* but is enhanced with negative *Nr*. In other words, assistive buoyancy damps the primary flow, whereas opposing buoyancy. This reduction weakens buoyancy-driven movement, tending to a decrease in fluid velocity. Consequently, with less buoyancy force driving fluid motion, the convective heat transfer process is hindered, resulting in depreciation of velocity profiles in the system. Fig.(11-12) demonstrates that an increment of *Nr* strengthens the buoyancy-driven flows. This

augmentation enhances fluid motion, facilitating more effective mixing and transport of heat and solute. Consequently, $\theta$, $\phi$ profile appreciates. Notably, both temperature $\theta$, concentration$\phi$ profiles show an upward trend, signifying that the heightened internal buoyancy forces improve heat, mass transfer. This results in higher thermal, solute gradients near the surface, causing increased $\theta$, $\phi$ levels within the boundary. Our outcomes align with the observed trends of Reddy *et al.*(2022), Anjum *et al.*(2025a), and (2025b). Physically, this signifies that stronger buoyancy effects lead to more efficient energy and species transport in the fluid. This is essential for precisely estimating flow behaviour and maximising mass and heat transfer in a variety of technical applications. $f'$ converges to a value close to 1 for all values of $Nr$. The convergence to this asymptotic value implies that beyond a certain point, further increases in $\eta$ have minimal effects on $f'$ This suggests that the system reaches a steady state or equilibrium condition.

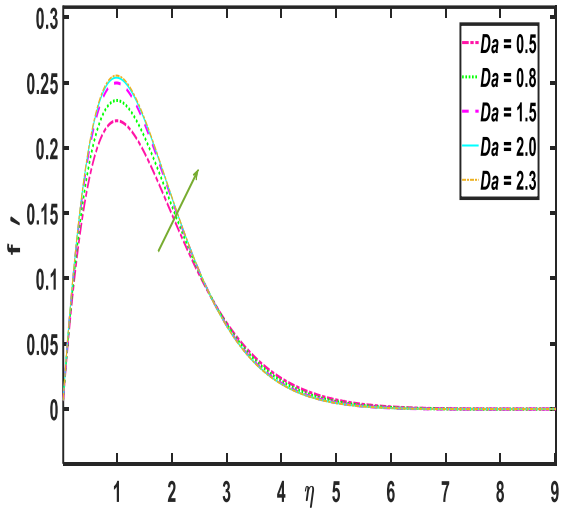


Fig. 13: Velocity description for *Da*.

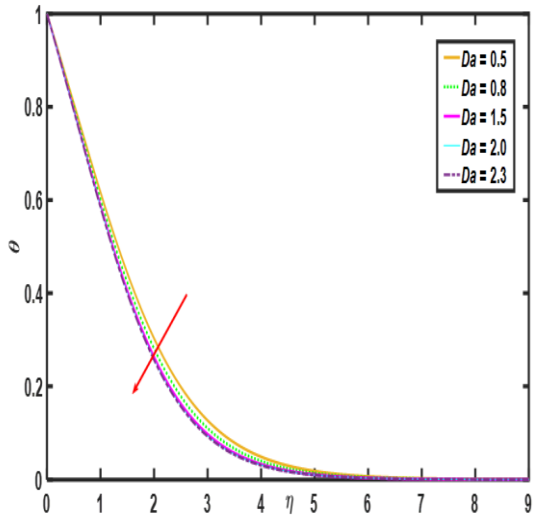


Fig. 14: Temperature description for *Da*.

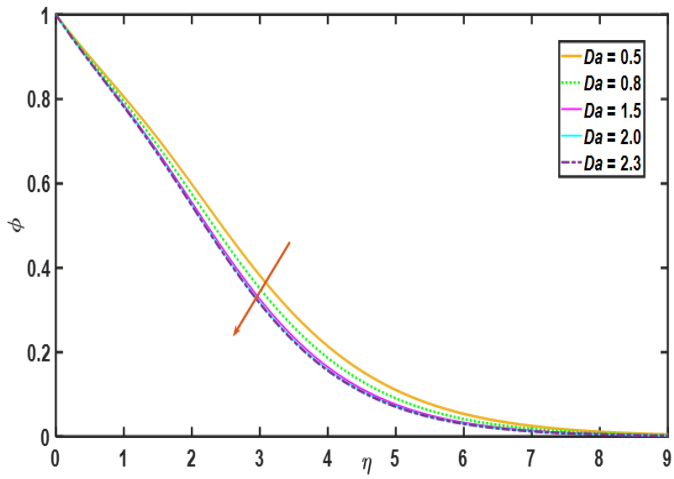


Fig. 15: Concentration description for *Da*

Figures ( 13 – 15 ) portray the impact of Darcy number *Da* on profiles $f'$, $\theta$, $\phi$. Fig. 13 demonstrates unambiguously that the velocity is much amplified with an increase in *Da*, with the maximum effect occurring close to the surface. Greater permeability, of course, indicates a decrease in solid Fibers that obstruct axial flow; this lowers the Darcian resistance and accelerates flow. Elevating pushes peak velocity even more *Da*. Fig. 14 shows that boosting the Darcy parameter yields a significant suppression of temperature. Heat conduction is suppressed as a result of the loss of solid fibers in the porous matrix linked to increased penetration. This cools the regime by reducing heat diffusion inside it. As a result, the surface's heat BLT is suppressed. Porous media with lower permeability reach far higher temperatures than those with higher permeability. Fig. 15 eluciates

that as the *Da* increases, this indicates increased resistance to flow through the porous medium. This resistance reduces the exchange of nanocrystals, leading to a low concentration of NPs near the surface. Consequently, overall,concentration $\phi$ profile within the fluid decreases. Physically, as *Da* increases, indicating higher permeability in the porous medium, the resistance to fluid flow decreases. This lower resistance allows for an increased fluid velocity because the flow encounters less drag. However, the enhanced fluid velocity leads to decay in both $\theta, \phi$ profiles. Essentially, fluid moves more quickly through the medium, carrying less heat and fewer NPs along with it. Reduced heat transmission via thermal conduction in the system is facilitated by the steady reduction of solid fibres that have large *Da* values in porous medium. This cools down the thermal BLT, which also diminishes and limits the transfer of thermal energy from the vertical surface into the system. As a consequence, the presence of porous materials significantly affects the system's speed and thermal dispersion, offering a solid foundation for regulating flow and temperature management". It is evident from equation (15) that the Darcian bulk impedance term has an inverse relationship with *Da*. Thus, the Darcian impedance arising from the viscous effect to stress at solid particle surfaces decreases dramatically with increasing *Da*. The flow experiences reduced matrix "resistance from the porous fibres, which become less common, with higher *Da* values (greater permeability). As a result, the flow quickens, its velocity rises, and the momentum of the regime does too. This parameter is crucial for analysing and modelling fluid flow behaviours in applications involving porous media, such as filtration, groundwater flow, and enhanced oil recovery.

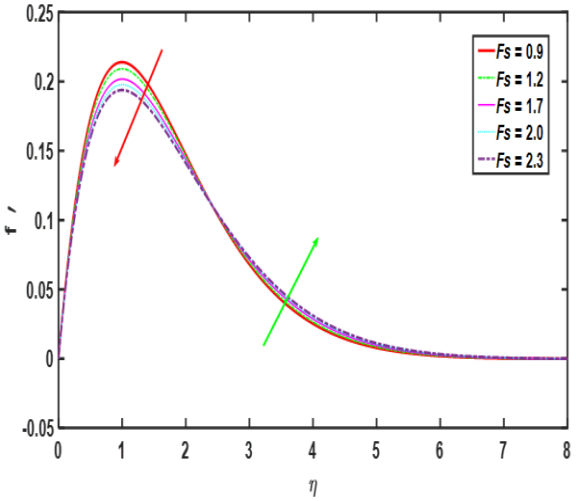


Fig. 16: Velocity description for *Fs*.

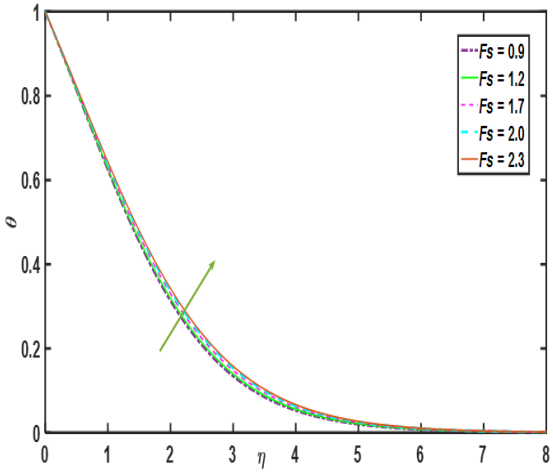


Fig. 17: Temperature description for *Fs*.

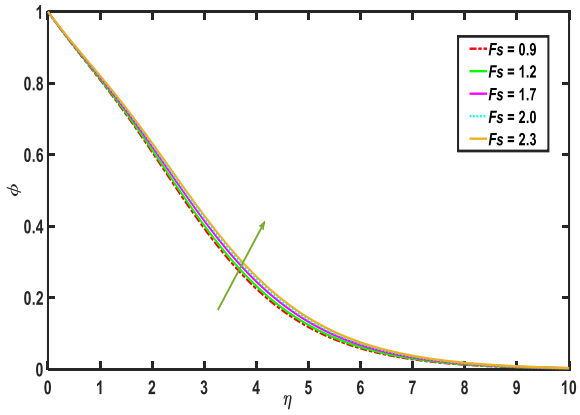


Fig. 18: Concentration description for *Fs*.

Figures (16–18) Emphasis impact of the Forchheimer number *Fs* on $f'$ $\theta, \phi$ profiles through the outermost regime with transverse coordinate $\eta$. Fig. 16 demonstrates how a greater inertial impedance that resists flow is present and causes a noticeable depreciation in velocity with an increase in *Fs*. This impact is maximised close to the surface; lesser deceleration in a flow with a higher *Fs* is calculated farther away. There is no discernible effect of *Fs* on flow in the free stream. Fig. 17 reveals that a significant heating impact occurs in the regime as a result of the higher *Fs*. Temperatures are always stronger for all transverse coordinate η values. Hence, the

thickness of thermal BL is highest for the strong Forchheimer case *Fs* = 1 and smallest for the weak Forchheimer drag case *Fs* = 0. Fig. 18 illustrates $\phi$ increases as *Fs* gradually rises because greater *Fs* signifies greater inertial effects in flow through a porous medium. These inertial effects enhance the mixing and dispersion of nanocrystals, leading to a greater concentration of NPs near the surface. Consequently, increased inertial forces facilitate better nanoparticle distribution and an elevated concentration profile. Our outcomes are consistent with the patterns of Reddy *et al*.(2022), Anjum *et al*.(2025a), (2025b). Physically, since the drag force and coefficient of inertia are connected, a surge in inertia causes the fluid's drag force to grow, thus lowering its speed. The influence of the quadratic inertial drag is larger with closer proximity to the wall's surface. Nevertheless, since Forchheimer drag is of order two, a rise in (*Fs)* virtually blanks the momentum development and causes a slowdown. Consequently, the reduced velocity decreases the convective heat transfer rate, resulting in higher temperatures near the surface. Simultaneously, the enhanced inertial effects promote better mixing and dispersion of NPs, increasing their concentration near the surface. Thus, $f'$ dampens while $\theta$, $\phi$ profiles enhance with higher Forchheimer numbers. *Fs* is used to optimize flow and performance in NF-based filtration systems and heat exchangers by accounting for inertial effects in porous media.

It is noteworthy that in Figs. (4 - 18 ) all ll profiles converge smoothly, validating the implementation of a sufficiently large infinity boundary condition in the free stream.

## 4. Conclusions

The non-similar, incompressible steady state laminar Darcy-Forchheimer convection flow of Buongiorno's Nanofluid past a Semi-Infinite vertical surface is investigated numerically. Thermal convection and nanoparticle mass transfer have also been investigated in the present paper. The conservation equations and BCs have been rendered dimensionless with appropriate scaling non-similarity transformations. While most studies focus on linear Darcy flows, this work extends the analysis to the nonlinear Da-Fs regime, capturing inertial effects that are crucial for high-velocity flows in porous media. filling a crucial gap in existing literature. The resulting nonlinear multi-physical boundary value problem has then been solved with realistic BCs, employing a second-order implicit finite-difference Keller Box technique. Graphical results for the influence of selected parameters on transport characteristics have been presented. A thorough evaluation of the impacts on thermofluidic properties has been conducted, considering the influence of *Nb*, *Nt*, *Nr*, *Da*, and *Fs* on $f'$, $\theta$, $\phi$ characteristics have been presented graphically. The implicit KBM has been validated with previous studies mentioned in the literature. From the above-mentioned results and discussion, the following conclusions can be drawn:

(i) As the Brownian motion parameter increases, velocity and temperature profiles are accelerated, whereas the concentration profile is dampened.

(ii) An increase in the thermophoresis parameter depletes the velocity profile, but temperature and concentration profiles are strongly improved

(iii) With a stronger Darcy number, it is noted that the velocity profile is enhanced close to the plate's surface, whereas temperature and concentration profiles decay significantly.

(iv) As the Forchheimer number value enhances, velocity reduces close to the plate's surface, whereas temperature and concentration profiles are strongly improved.

(v) A heightened Buoyancy ratio parameter strengthens buoyancy-driven flows, declines the velocity profile and enhances temperature and concentration profiles.

The current investigation has uncovered some intriguing traits of semi-infinite vertical substrate nanofluid BL flows. The combined analysis of Buongiorno's nanofluid model and Darcy-Forchheimer drag's combined effects on non-similar convection flows across a semi-infinite vertical plate constitutes the innovations of this work. Moreover, velocity, temperature, and concentration profiles are thoroughly examined graphically for various parameters and partial differential equations, which encompass fully two-dimensional nanofluid flow. These weren't taken into consideration in previous investigations. The effectiveness of KBM in resolving these intricate multi-physical BVPs has been demonstrated. But only the Newtonian example has received attention. It is well known that NFs with a higher volume proportion of nanoparticles show rheological effects.

## 5. Future Scope

Future research can extend this study by incorporating variable thermophysical properties and exploring unsteady flow conditions to better simulate real-world applications. Investigating the effects of different

nanoparticle shapes and base fluids could enhance the accuracy of NF models. Additionally, implementing machine learning techniques for parameter optimization in heat transfer applications may provide further advancements. Experimental validation of the numerical findings would also strengthen the reliability of the proposed model. Future research could thus examine non-Newtonian polymeric models, such as shear-thinning and viscoelastic formulations. Additionally, studying NF behavior in complex geometries and incorporating detailed boundary conditions, including time-dependent effects, could better simulate practical scenarios. Leveraging advanced computational techniques, such as machine learning and high-performance computing, will further refine simulations and predict nanofluid dynamics under extreme conditions, which will be communicated soon.

## Credit author statement:

**Dr. Samdani:** Software, editing, Visualizations, **Dr. Shaik Abdul Gaffar:** Conceptualization, Problem formulation, solving, Software, **Dr. Asra Anjum:** Problem formulation, original drafting, editing, and Software.

## Acknowledgments

The authors appreciate the reviewers' and editor's perceptive comments, encouraging words, and practical suggestions for improving the original work, all of which have assisted us in revising the final version of the manuscript.

## References

Anjum, N., Khan, W. A., Hobiny, A., Azam, M., Waqas, M., & Irfan, M. (2022). Numerical analysis for thermal performance of modified Eyring Powell nanofluid flow subject to activation energy and bioconvection dynamics. Case Studies in Thermal Engineering, 39, 102427. https://doi.org/10.1016/j.csite.2022.102427

Anjum, A., Gaffar, S. A., Kumar, D. S., Bég, O. A., & Peerusab, S. (2024). Non-similar Keller box analysis of magnetically radiative Buongiorno's nanofluid flows past a stretching surface. Journal of Naval Architecture and Marine Engineering, 21(2), 127–153. https://doi.org/10.3329/jname.v21i2.74923

Anjum, A., Gaffar, S. A., Kumar, D. S., & Peerusab, S. (2025). A numerical analysis of convection flows of Buongiorno's nanofluid past an elongating sheet with multiple slip effects. Journal of Naval Architecture and Marine Engineering, 22(2), 117-140. https://banglajol.info/index.php/JNAME/article/view/79532

Gaffar, S. A., Bég, O. A., Anjum, A., Bég, T. A., Leonard, H. J., Kuharat, S., & Reddy, R. P. (2025). Simulating magneto-convective radiative nanofluid flow from a non-isothermal rotating cone with heat generation and chemical reaction. Journal of Nanofluids, 14(3), 447-465. https://doi.org/10.1166/jon.2025.2244

Amanulla, C. H., Nagendra, N., & Suryanarayana Reddy, M. (2018). Computational analysis of non-Newtonian boundary layer flow of nanofluid past a semi-infinite vertical plate with partial slip. Nonlinear Engineering, 7(1), 29-43. https://doi.org/10.1515/nleng-2017-0055.

Anjum, A., Gaffar, S. A., Kumar, S., & Peerusab, S. (2025a). Dissipative magneto-thermo-convection of nanofluid past through a Semi-Infinite vertical surface with ohmic heating. Journal of Applied and Computational Mechanics, 11(4), 991-1008. https://doi.org/10.22055/jacm.2024.47689.4765

Anjum, A., Kumar, D. S., Gaffar, S. A., & Peerusab, S. (2025b). Heat and mass transfer in magneto-dissipative Buongiorno nanofluid flow along a semi-infinite plate in a non-Darcy porous medium. International Journal of Heat & Technology, 43(2). https://doi.org/10.18280/ijht.430220

Ali, M., Nasrin, R., & Alim, M. A. (2021). Analysis of boundary layer nanofluid flow over a stretching permeable wedge-shaped surface with magnetic effect. Journal of Naval Architecture and Marine Engineering, 18(1), 11-24.

Bhavani,D. J., Gopal, S.T., Gnanasekar, S., Pandiaraj, S., Muthuramamoorthy, M., Alodhayb, A. N., & Andrews, N. G. Case Studies in Thermal Engineering. https://doi.org/10.1016/j.csite.2024.104120.

Buongiorno, J. (2006). Convective transport in nanofluids. https://doi.org/10.1115/1.2150834.

Bég, O. A. (2013). Numerical methods for multi-physical magnetohydrodynamics. Journal of Magnetohydrodynamics and Plasma Research, 18(2/3), 93.

Choi, S. U., & Eastman, J. A. (1995). Enhancing thermal conductivity of fluids with nanoparticles (No. ANL/MSD/CP-84938; CONF-951135-29). Argonne National Lab. (ANL), Argonne, IL (United States).

Cui, J., Munir, S., Farooq, U., Rabie, M. E. A., Muhammad, T., & Razzaq, R. (2021). On numerical thermal transport analysis of three-dimensional bioconvective nanofluid flow. Journal of Mathematics, 2021(1), 5931989. https://doi.org/10.1155/2021/5931989.

Chamkha, A. J., & Aly, A. M. (2010). MHD free convection flow of a nanofluid past a vertical plate in the presence of heat generation or absorption effects. Chemical Engineering Communications, 198(3), 425-441. https://doi.org/10.1080/00986445.2010.520232.

Farooq, U., Razzaq, R., Khan, M. I., Chu, Y. M., & Lu, D. C. (2021). Modeling and numerical computation of nonsimilar forced convective flow of viscous material towards an exponential surface. International Journal of Modern Physics B, 35(08), 2150118. https://doi.org/10.1142/S0217979221501186.

Forchheimer, P. H. (1901). Wasserbewegung. Ver. Dtsch. Ing., 45, 1782-1788.

Gebhart, B., Jaluria, Y., Mahajan, R. L., Sammakia, B., & Yovanovich, M. M. (1989). Buoyancy-induced flows and transport. https://doi.org/10.1115/1.3226555

Gebhart, B., & Pera, L. (1971). The nature of vertical natural convection flows resulting from the combined buoyancy effects of thermal and mass diffusion. International Journal of Heat and Mass Transfer, 14(12), 2025-2050. https://doi.org/10.1016/0017-9310(71)90026-3.

Gangadhar, K., Kumari, M. A., & Chamkha, A. J. (2022). EMHD flow of radiative second-grade nanofluid over a Riga Plate due to convective heating: Revised Buongiorno's nanofluid model. Arabian Journal for Science and Engineering, 47(7), 8093-8103. https://doi.org/10.1007/s13369-021-06092-7

Gaffar, S. A., Bég, O. A., Kuharat, S., & Bég, T. A. (2024). Computation of hydromagnetic tangent hyperbolic non-Newtonian flow from a rotating non-isothermal cone to a non-Darcy porous medium with thermal radiative flux. Physics Open, 19, 100216. https://doi.org/10.1016/j.physo.2024.100216.

Humane, P. P., Patil, V. S., Patil, A. B., & Shamshuddin, M. D. (2023). Buongiorno modelled nanoliquid consequence of thermal and solutal convection on the Magneto-micropolar fluid inside an inclined porous stretching device. Journal of Nanofluids, 12(1), 211-222. https://doi.org/10.1166/jon.2023.1949.

Hussain, M., Imran, M., Waqas, H., Muhammad, T., & Eldin, S. M. (2023). An efficient heat transfer analysis of MHD flow of hybrid nanofluid between two vertically rotating plates using the Keller box scheme. Case Studies in Thermal Engineering, 49, 103231. https://doi.org/10.1016/j.csite.2023.103231.

Hossain, M. M., Nasrin, R., & Hasanuzzaman, M. (2024). Unsteady magneto-porous convective transport by micropolar binary fluid due to inclined plate: An inclusive analogy. Heliyon, 10(2).

Khatun, S., & Nasrin, R. (2021). Numerical modeling of Buongiorno's nanofluid on free convection: thermophoresis and Brownian effects. Journal of Naval Architecture and Marine Engineering, 18(2), 217-239.

Khan, A. W., 2022. Impact of time-dependent heat and mass transfer phenomenon for magnetized Sutterby nanofluid flow. *Waves in random and complex media*, pp.1-15.https://doi.org/10.1080/17455030.2022.2140857

Khan, W. A. (2023). Significance of magnetized Williamson nanofluid flow for ferromagnetic nanoparticles. Waves in Random and Complex Media, 1-20.https://doi.org/10.1080/17455030.2023.2207390

Khan, Z. H., Makinde, O. D., Usman, M., Ahmad, R., Khan, W. A., & Huang, Z. (2023). Inherent irreversibility in unsteady magnetohydrodynamic nanofluid flow past a slippery permeable vertical plate with fractional-order derivative. Journal of Computational Design and Engineering, 10(5), 2049-2064. https://doi.org/10.1093/jcde/qwad090

Keller, H. B. (1978). Numerical methods in boundary-layer theory. Annual Review of Fluid Mechanics, 10, 417-433. https://doi.org/10.1146/annurev.fl.10.010178.002221.

Khan, B. M. H., Gaffar, S. A., Beg, O. A., Kadir, A., & Reddy, P. R. (2020). Computation of Eyring-Powell micropolar convective boundary layer flow from an inverted non-isothermal cone: thermal polymer coating simulation. Computational Thermal Sciences: An International Journal, 12(4). https://doi.org/10.1615/ComputThermalScien.2020033860

Khan, W. A. (2023). Dynamics of gyrotactic microorganisms for modified Eyring Powell nanofluid flow with bioconvection and nonlinear radiation aspects. Waves in Random and Complex Media, 1-11. https://doi.org/10.1080/17455030.2023.2168086

Khan, Z. H., Makinde, O. D., Trounev, A., Khan, W. A., & Ahmad, R. (2024). Entropy generation and heat transfer in Time-Fractional mixed convection of nanofluids in Darcy-Forchheimer porous channel. Engineering Science and Technology, an International Journal, 60, 101908. https://doi.org/10.1016/j.jestch.2024.101908

Kuznetsov, A. V., & Nield, D. A. (2010). Natural convective boundary-layer flow of a nanofluid past a vertical plate. International Journal of Thermal Sciences, 49(2), 243-247. https://doi.org/10.1016/j.ijthermalsci.2009.07.015.

Muskat, M., & Wyckoff, R. (1946). The Flow of Homogeneous Fluids Through Porous Media: Ann Arbor. Michigan, JW Edwards, 763.

Makinde, O. D., Khan, Z. H., Trounev, A., Khan, W. A., & Ahmad, R. (2024). Fractional dynamics of entropy generation in unsteady mixed convection of a reacting nanofluid over a slippery permeable plate in Darcy–Forchheimer porous medium. ZAMM-Journal of Applied Mathematics and Mechanics/Zeitschrift für Angewandte Mathematik und Mechanik, 104(9), e202400083. https://doi.org/10.1002/zamm.202400083

Nadeem, S., Ijaz, M., & Ayub, M. (2021). Darcy–Forchheimer flow under rotating disk and entropy generation with thermal radiation and heat source/sink. Journal of Thermal Analysis and Calorimetry, 143(3), 2313-2328. https://doi.org/10.1007/s10973-020-09737-1.

Narahari, M. (2018, April). Unsteady free convection flow past a semi-infinite vertical plate with constant heat flux in water-based nanofluids. In IOP Conference Series: Materials Science and Engineering (Vol. 342, No. 1, p. 012085). IOP Publishing. https:// 10.1088/1757-899X/342/1/012085

Razzaq, R., Farooq, U., Cui, J., & Muhammad, T. (2021). Non-similar solution for magnetized flow of Maxwell nanofluid over an exponentially stretching surface. Mathematical Problems in Engineering, 2021(1), 5539542. https://doi.org/10.1155/2021/5539542.

Reddy, R. P., Gaffar, S. A., Beg, O. A., & Khan, B. M. H. (2022). Hall and ion-slip effects on nanofluid transport from a vertical surface: Buongiorno's model. ZAMM-Journal of Applied Mathematics and Mechanics/Zeitschrift für Angewandte Mathematik und Mechanik, 102(3), e202000174. https://doi.org/10.1002/zamm.202000174.d

Razzaq, R., & Farooq, U. (2021). Non-similar forced convection analysis of Oldroyd-B fluid flow over an exponentially stretching surface. Advances in Mechanical Engineering, 13(7), 16878140211034604. https://doi.org/10.1177/16878140211034604.

Raees, A., Farooq, U., Hussain, M., Khan, W. A., & Farooq, F. B. (2021). Non-similar mixed convection analysis for magnetic flow of second-grade nanofluid over a vertically stretching sheet. Communications in Theoretical Physics, 73(6), 065801. https://doi10.1088/1572-9494/abe932.

Reddy, R., & Gaffar, S. A. (2024). Chemical Reaction and Viscous Dissipative Effects on Buongiorno's nanofluid model Past an inclined plane: A Numerical Investigation. International Journal of Applied and Computational Mathematics, 10(2), 81. http://dx.doi.org/10.1007/s40819-024-01723-7.

Sparrow, E. M., Quack, H., & Boerner, C. J. (1970). Local nonsimilarity boundary-layer solutions. AIAA journal, 8(11), 1936-1942. https://doi.org/10.2514/3.6029

Sparrow, E. M., & Yu, H. S. (1971). Local non-similarity thermal boundary-layer solutions. https://doi.org/10.1115/1.3449827.

Shaheen, A., Waqas, H., Imran, M., Raza, M., & Rashid, S. (2024). The effects of thermal radiation and heat source/sink on the flow and heat transfer characteristics of a hybrid nanofluid over a vertical stretching cylinder: Regression analysis. International Journal of Modern Physics B, 38(29), 2450397. https://doi.org/10.1142/S0217979224503971

Saeed, A., Tassaddiq, A., Khan, A., Jawad, M., Deebani, W., Shah, Z., & Islam, S. (2020). Darcy-Forchheimer MHD hybrid nanofluid flow and heat transfer analysis over a porous stretching cylinder. Coatings, 10(4), 391. https://doi.org/10.3390/coatings10040391.

Siddiqa, S., Begum, N., Hossain, M. A., Abrar, M. N., Gorla, R. S. R., & Al-Mdallal, Q. (2021). Effect of thermal radiation on conjugate natural convection flow of a micropolar fluid along a vertical surface. Computers & Mathematics with Applications, 83, 74-83. https://doi.org/10.1016/j.camwa.2020.01.011

Usman, M., Haq, R. U., Hamid, M., Lu, D., & Zhang, Z. (2024). Natural convection role in MHD flow of heat exchange inside a wavy cavity. International Communications in Heat and Mass Transfer, 159, 108250. https://doi.org/10.1016/j.icheatmasstransfer.2024.108250.

Uddin, M. J., Nasrin, R., & Alatawi, E. S. (2025). Augmenting thermal-material transport in boundary-layer flow over an upright sheet: An explicit finite difference approach. Journal of Naval Architecture and Marine Engineering, 22(1), 21-40.

Vedavathi, N., Dharmaiah, G., Abdul Gaffar, S., & Venkatadri, K. (2021). Entropy analysis of nanofluid magnetohydrodynamic convection flow past an inclined surface: a numerical review. Heat Transfer, 50(6), 5996-6021. https://doi.org/10.1002/htj.22159

Waqas, M., Khan, W. A., Pasha, A. A., Islam, N., & Rahman, M. M. (2022). Dynamics of bioconvective Casson nano liquid from a moving surface capturing gyrotactic microorganisms, magnetohydrodynamics, and stratifications. Thermal Science and Engineering Progress, 36, 101492.
https://doi.org/10.1016/j.tsep.2022.101492

Wang, F., Saeed, A. M., Puneeth, V., Shah, N. A., Anwar, M. S., Geudri, K., & Eldin, S. M. (2023). Heat and mass transfer of Ag–H2O nano-thin film flowing over a porous medium: A modified Buongiorno's model. Chinese Journal of Physics, 84, 330-342. https://doi.org/10.1016/j.cjph.2023.01.001.

Waqas, H., Farooq, U., Yang, S., Muhammad, T., & Imran, M. (2023). Heat transfer aspects in Carreau nanofluid having hybrid nanoparticles through a porous medium. ZAMM-Journal of Applied Mathematics and Mechanics/Zeitschrift für Angewandte Mathematik und Mechanik, 103(3), e202100414. https://doi.org/10.1002/zamm.202100414

Yahyaee, A., Hærvig, J., & Sørensen, H. (2024). Nanoparticle migration in nanofluid film boiling: A numerical analysis using the continuous-species-transfer method. International Journal of Heat and Mass Transfer, 224, 125344. https://doi.org/10.1016/j.ijheatmasstransfer.2024.125344.